ACS Photonics

pubs.acs.org/journal/apchd5

Article

Attoliter Mie Void Sensing

Serkan Arslan,* Micha Kappel, Adrià Canós Valero, Thi Thu Huong Tran, Julian Karst, Philipp Christ, Ulrich Hohenester, Thomas Weiss, Harald Giessen, and Mario Hentschel

Cite This: https://doi.org/10.1021/acsphotonics.5c01198

Read Online

ACCESS | Metrics & More | Article Recommendations | Supporting Information

ABSTRACT: Traditional nanophotonic sensing schemes utilize evanescent fields in dielectric or metallic nanoparticles, which confine far-field radiation in dispersive and lossy media. Apart from the lack of a well-defined sensing volume, these structures suffer from the generally limited access to the modal field, which is one key aspect for sensing performance. Recently, a novel strategy for dielectric nanophotonics has been demonstrated, namely, the resonant confinement of light in air. So-called Mie voids created in high-index dielectric host materials support localized resonant modes with exceptional properties. In particular, these structures benefit from the full access to the modal field confined strongly inside the void. We utilize these Mie voids for refractive index sensing in single voids with volumes down to 100 attoliters and sensitivities on the order of 400 nm per refractive index unit. Taking the noise of our measurements into account, we demonstrate detection of refractive index changes as small as 1×10^{-3} in a defined volume of just 390 attoliters. The combination of our Mie void sensor platform with appropriate surface functionalization will even enable specificity to biological or other analytes of smallest volumes while maintaining said sensitivity.

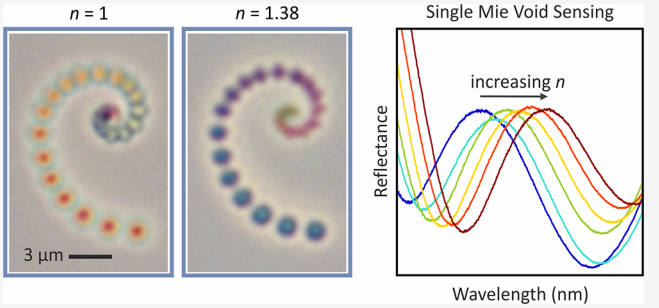

KEYWORDS: *nanophotonic sensing, Mie void, bio sensor*

INTRODUCTION

Sensing applications have been a key driving force behind nanophotonics and plasmonics[1−4] and include medical demands such as the detection of biomolecules and their conformational changes,[5−8] safety-related concerns such as the measurement of gas concentrations, monitoring of chemical reactions,[9] and many more.[10−16] Ultimately, achieving the highest sensitivities for smallest quantities, possibly even down to single biomolecules, requires optimization of the sensing platform.[17−29] Optimization, however, depends on the sensing application.[30−35] While the quality factor of the resonances is important to discriminate spectral shifts, also the mode volume has to be taken into account in order to optimize the sensor performance.[36−42] While exhibiting excellent sensitivity and performance,[43−45] highest quality factors are often observed for extended modes in gratings or periodic structures, resulting in very large sensing volumes. In other cases, high-quality factors are associated with strongly confined modes, hampering interaction with materials of interest.[46] Direct comparison between plasmonic and dielectric resonances has shown that sensitivities of dielectric structures can be lower, yet, still offer benefits in terms of linearity of the response and CMOS integrability, again underpinning the importance of the application at hand.[47] Combining whispering gallery modes resonators with, e.g., plasmonic nanoantennas is another powerful alternative approach.[48−50]

Additionally, pushing a sensor to the ultimate limit can also mean reaching an ultimately small sensing volume. In this letter we introduce Mie voids as a novel sensing platform, making use of the unique full accessibility of their modal fields.[51,52] Mie voids, which are void structures in high refractive index dielectrics that strongly confine light, are thus ideal candidates for nanoscale optical sensing as they maximize the far-field response by maximizing the analyte-resonator interaction in a well-defined and extremely small volume.[51,53] The optical response is in fact so large that the change in optical properties of individual resonators can be observed with bare eyes in an optical microscope. Ultimately, we demonstrate that single Mie voids can report refractive index changes as small as 1×10^{-3} inside a volume of only 390 attoliters. We note that these sensitivities are below flat-film SPR and other extended mode sensing platforms, which, conversely, cannot address ultimately small volumes.[54,55] While plasmonic nanohole arrays have been widely used for refractive index sensing,[56−58] demonstrations of single plasmonic

Received: May 28, 2025
Revised: June 11, 2025
Accepted: June 11, 2025

nanohole sensors remain relatively rare. Some studies have explored single nanoholes to detect individual molecules or particles, such as virus-like particles[59] and DNA translocation events.[60] However, these approaches typically focus on qualitative detection or analyte trapping rather than high-resolution, quantitative refractive index measurements. In contrast, our dielectric Mie void platform enables robust, label-free refractive index sensing at the attoliter scale with high signal-to-noise performance. This distinguishes our work from plasmonic approaches and highlights its potential for ultra-miniaturized, quantitative sensing. In addition, Mie void sensors in gallium arsenide or silicon can be fabricated by standard semiconductor nanolithography process lines. Beyond the current experiments, surface functionalization can introduce selectivity to specific analytes and allow for their discrimination. Mie voids are also ideal as a platform for microfluidic sensing chips due to the ease of fabricating voids in, e.g., silicon substrates and their straightforward integrability into this platform.[16,61,62]

Concept. Figure 1a illustrates the basic concept of Mie void sensing. The artistic sketch depicts a single Mie void in a gallium arsenide surface. Such a void supports resonant modes, confining the radiation to the void region, which allows full access to the modal field distributions.[63] Counterintuitively, it has been shown the nearly the entire modal field distribution is confined to the air void, with barely any penetration into the surrounding material. Mie voids are thus an ideal nanoscale sensor for liquid analytes, serving not only as the analyte container of well-defined volume but also supporting a localized resonant mode and thus ensuring maximized interaction, providing a distinct benefit over solid nano-resonators or nanoparticles. In the experiment, we collect white light reflection spectra from the structures, and record the changes to the optical response for different analytes. The setup allows us to measure the reflectance spectra of arrays of Mie voids as well as individual ones.

Figure 1b depicts the basic working principle. The leftmost scanning electron microscopy (SEM) images show arrangements of individual Mie voids of varying diameter and nominally identical depth. The top depicts a spiral of voids with continuously increasing diameter, and the bottom one displays a random arrangement of voids with different diameters. The middle and rightmost columns depict optical microscope images of the same arrangement of voids in air and a liquid surrounding of refractive index n = 1.38 (propanol). One can clearly observe the resonant scattering of the individual voids in dependence on their diameter. This manifests itself as a significant color change, that is, resonance shift for different refractive index surroundings. The images for the air and liquid surroundings reveal a very strong color change from an orange-to-red-dominated hue for air-filled to a purple-to-blue-dominated one for the propanol-filled voids.

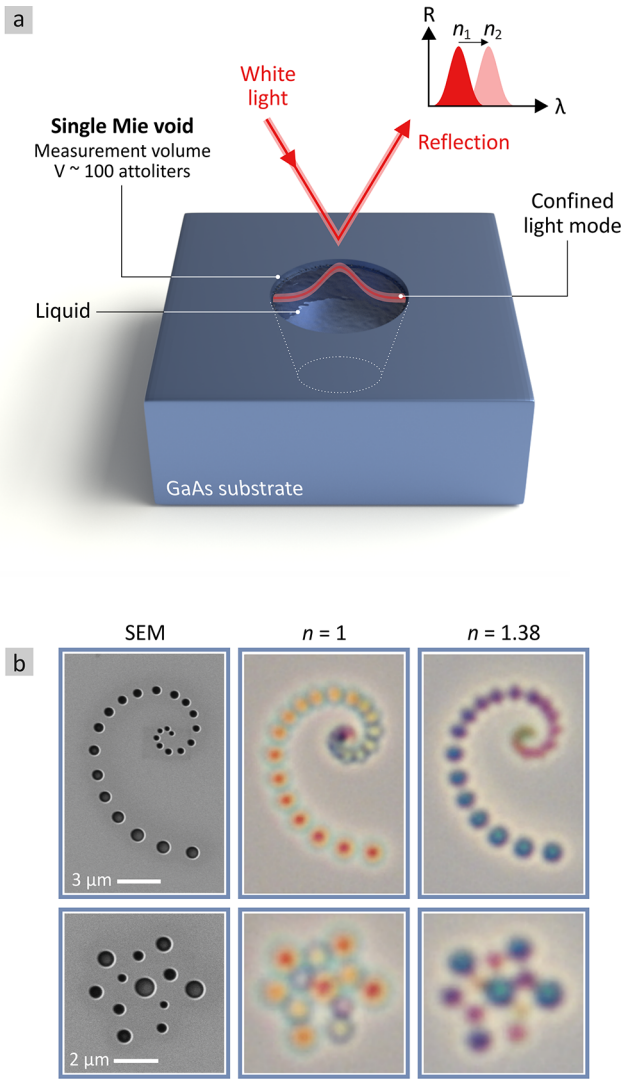

Figure 1. (a) Basic idea of Mie void-based sensing. The well-defined volume of the resonant nanostructure makes a Mie void an ideal nanoscale sensor, maximizing interaction of the analyte with the localized mode inside the void. (b) Scanning electron microscopy (SEM) images and optical micrographs of arrangements of individual Mie voids with different sizes and thus different resonance positions. Each void is associated with a distinct color impression. Changing the refractive index of the surrounding from 1 to 1.38 for propanol causes the spectral resonance to shift dramatically, underpinning the working mechanism of the Mie void sensor.

METHODS

The measurement setup is sketched in Figure 2a. We perform refractive index measurements of liquids inside a flow cell with a source and drain to flush the cell with liquids, in this case, propanol and toluene with n = 1.38 and 1.49, respectively. These values stem from taking the average value of the refractive index dispersion between 500 and 1000 nm.[64,65] By choosing an appropriate mixture of the two liquids, we can interpolate refractive indices between these two extreme values. In the experiment, we utilize mixing ratios of (10:0, 8:2, 6:4, 4:6, 2:8, 0:10), corresponding to refractive indices of (1.380, 1.402, 1.424, 1.446, 1.468, 1.490), providing a well-defined and tunable experimental system to study the sensing characteristics of this platform. Through a glass window in our cell, the Mie void sample can be imaged with a 60× Nikon objective which is part of a microspectroscopy setup based on an inverse Nikon TE2000-U microscope.[26,66] As the substrate is intransparent, we measure reflectance spectra in a bright-field geometry. For this, we utilize Köhler illumination and collect the reflected light with the help of a 4f setup coupled to a Princeton Instruments grating spectrometer (SP2500i). Both the illumination and collection paths utilize apertures in the Fourier plane (A-stop) in order to limit the illumination and collection to angles close to normal incidence, effectively reducing the NA of the objective to approximately 0.14. This is

https://doi.org/10.1021/acsphotonics.5c01198
ACS Photonics XXXX, XXX, XXX−XXX

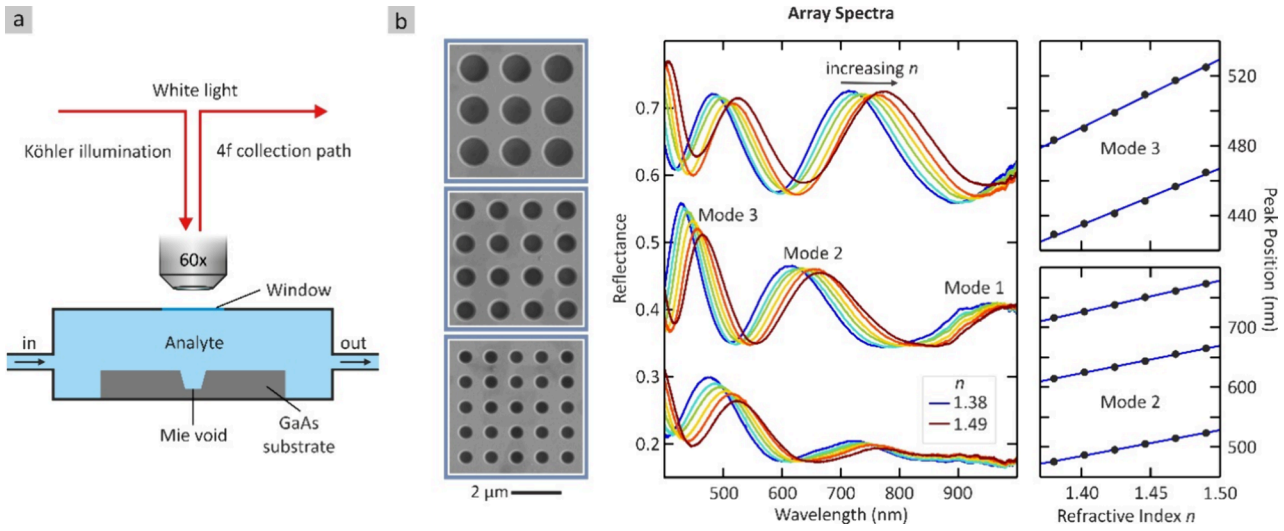

Figure 2. (a) Sketch of the measurement setup consisting of a fluid cell for the exchange of different analytes with different refractive indices as well as the illumination and collection path of the white light reflection measurement. (b) SEM micrographs as well as reflectance spectra for different arrays of Mie voids and the extracted shifts of the modal features with their associated linear regressions. The top radii of the voids are 265, 395, and 570 nm, with a nominally identical depth of 480 nm. The spectra for the two larger radii have been shifted upward for clarity (by 0.225 and 0.5, respectively).

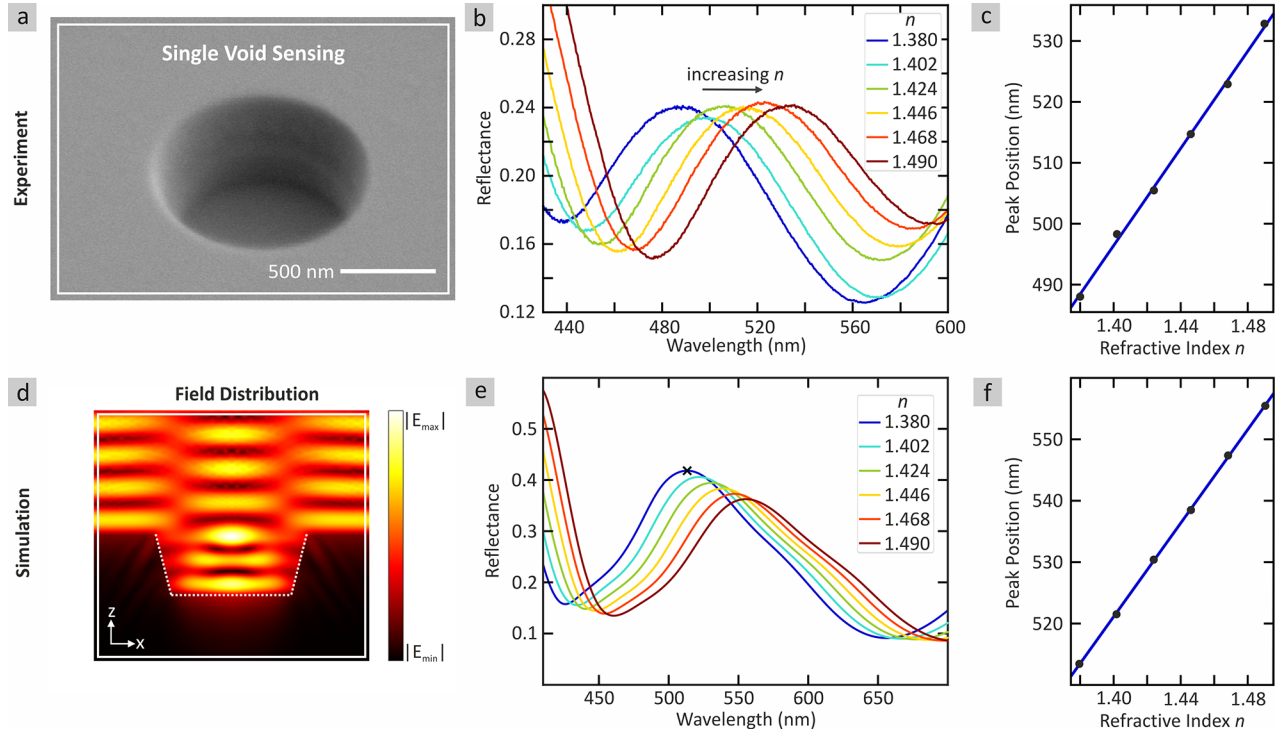

Figure 3. Single Mie void refractive index sensing. (a) 45° tilted-view SEM image of the used Mie void. (b) Reflectance spectra for different analyte solutions. (c) Extracted peak position with respect to the corresponding refractive index and a linear fit. (d) Simulated electric field intensity distribution for a void filled with analyte of refractive index 1.38 at a wavelength of 513 nm (resonance peak). (e) Simulated single Mie void reflectance spectra. (f) Extracted peak positions for the simulated spectra.

necessary as Mie void reflectance spectra are highly angle dependent also preventing the usage of dark-field spectroscopy. As we measure in bright-field reflectance geometry, we use an aperture in the image plane of the collection path (F-stop) to only collect light from the region of interest (arrays or single voids). For the single void measurements, we utilize fixed-size apertures in the collection path. For the 60× objective, pinholes of 150 μm, 100 μm, or 75 μm diameter were used depending on the void size (further details in the Supporting Information, Figure S7).

RESULTS AND DISCUSSION

Figure 2b presents reflectance spectra for different analyte combinations. All spectra presented in this work are plotted as absolute reflectance by normalizing the Mie void signal to the measured reflectance of the adjacent GaAs substrate and

https://doi.org/10.1021/acsphotonics.5c01198
ACS Photonics XXXX, XXX, XXX−XXX

subsequently multiplying by the known reflectance dispersion of GaAs. The data shown corresponds to three different arrays of voids with different radii as displayed in the SEM images to the left. The void radii are 265, 395, and 570 nm, respectively (top radius) with nominally identical depths of 480 nm. The middle panel shows the reflection spectra in a waterfall plot in dependence of the different analyte refractive indices.

We first consider the general shape of the measured reflectance spectra. Looking at the sweep in the middle corresponding to the medium-sized voids we observe the distinct resonant peak features of the three lowest-order Mie void modes, labeled as modes 1 to 3. In comparison, these modal features are blue-shifted in the spectra of the smaller voids at the bottom, where only modes 1 and 2 are observable. Conversely, in the spectra of the biggest voids at the top, the modes are red-shifted with modes 2 and 3 being clearly visible and parts of mode 4 shifting into the visible range above 400 nm.

We now turn our attention to the resonance shifts upon exchange of the analytes. For all three arrays, we observe a clear red shift for increasing refractive indices, as expected. In order to analyze these wavelength shifts in detail, we extract the peak positions from the spectra and plot them over the corresponding refractive index in the right column of Figure 2b. As only the modes 2 and 3 are entirely within the measurable wavelength range, we focus our discussion on these. For all three void sizes, a clear linear dependence between peak position and refractive index can be observed for both modes. This result is intuitive as the refractive index increases the optical path length and therefore the effective resonator size, thus lowering the energy of a given mode. By fitting linear functions, we obtain the sensitivity for the different void sizes and mode orders from these data. We define sensitivity as wavelength shift of peak position per refractive index unit (RIU). For mode 2 from biggest to smallest void the slopes are $\Delta\lambda/\Delta n = (523 \pm 7)$nm/RIU, $\Delta\lambda/\Delta n = (459 \pm 9)$nm/RIU and $\Delta\lambda/\Delta n = (433 \pm 8)$nm/RIU. For mode 3 the biggest void exhibits a sensitivity of $\Delta\lambda/\Delta n = (391 \pm 10)$nm/RIU and the medium sized one $\Delta\lambda/\Delta n = (323 \pm 12)$nm/RIU. The listed errors are the estimated parameter error of the linear fits. Additional array measurements for further void sizes can be found in the Supporting Information, Figure S1.

One key feature of Mie void sensing is the well-defined and ultrasmall sensing volume of the single void, which is only on the order of a few hundred attoliters. This intriguing property can only be fully exploited when addressing a single Mie void. Results in Figure 1b already indicate that individual voids are clearly observable in a microscope with naked eye, thus it appears more than feasible to also extract the spectral information.

For these measurements, we have chosen the Mie void depicted in the SEM image in Figure 3a with a volume of ~370 attoliters (550 nm top radius, 435 nm bottom radius, 480 nm depth). For this individual Mie void, Figure 3b displays the reflectance spectra recorded for the same set of refractive indices as before. Despite the fact that we are addressing a single Mie void and thus interrogate only an analyte volume of 370 attoliters, we observe well-modulated spectra with an excellent average signal-to-noise ratio of 182 (calculated as the ratio of peak prominence (0.0729) over noise (0.0004), where noise is defined as the standard deviation of the measured data points from a high order polynomial fit of the spectra). We note that the peak prominence and modulation depends on the pinhole size chosen in the experiment as this determines the ratio between void signal and background (for more details see Figure S7). As expected, the spectra undergo a red shift for increasing refractive indices. We extract the peak position for each refractive index step and plot it as a function of the corresponding refractive index in Figure 3c, which shows the expected linear dependence. The fit returns a sensitivity of $\Delta\lambda/\Delta n = (399 \pm 7)$nm/RIU. We thus observe similar sensitivities compared to the array measurements, corroborating the fact that voids only interact very weakly with each other. The presented error in sensitivity again only signifies the estimated parameter error of the linear fit. In addition we extract the average line width of the six measured peaks as the full width at half prominence to be of 58.4 nm which allows the calculation of the figure of merit FOM = 6.8/RIU defined as sensitivity (nm/RIU) over line width (nm).

In order to further underpin our results, we performed full-wave simulations with the Finite Element Method implemented in COMSOL Multiphysics, (Figure 3d,e). Figure 3d displays the absolute value of the electric field at the resonance wavelength. Three field maxima can be observed within the void, confirming the excitation of a high order mode of the resonator, in contrast with the low order modes investigated previously.[51] The simulated reflectance spectra are depicted in Figure 3e and show good agreement with the measurements. Deviations in the absolute position of the peaks likely occur due to differences between simulated and real void dimensions. As we are here interested in a general understanding of the observed phenomena only, we considered in our simulations the nominal void dimensions without performing any fine-tuning of parameters. Figure 3f depicts the simulated shift of the peak position against the corresponding refractive index. The sensitivity of $\Delta\lambda/\Delta n = (381 \pm 4)$nm/RIU is in good agreement with the measurement.

Another important cross-check is related to the actual active sensing volume. In our experiment not only the void itself but also the volume above the sample is filled with the analyte. In order to investigate its impact, we performed simulations assuming only the void filled, void and space above filled, and an empty void with filled space above (see Supporting Information Figure S2). The simulations clearly prove that a spectral shift of the features is only observed for an analyte-filled void and is barely influenced by the analyte above the sample.

The sensing volume can be further decreased by using smaller-sized Mie voids. To illustrate this, Figure S3 in the Supporting Information presents measurements for a Mie void with a volume of only 100 attoliters, still offering good sensing performance with a sensitivity of $\Delta\lambda/\Delta n = (516 \pm 13)$nm/RIU. Two constraints must be considered here: First, the resonances will blue-shift, at ultimate small sizes toward the UV spectral range, which is outside of the easy-to-access spectral range. Second, the coupling of the modes with the far field will decrease due to the decreased volume and thus diminish the observable signal-to-noise ratio.

Utilizing a sensing platform with ultimate small sensing volumes on the order of a few hundred attoliters becomes particularly interesting when pushing it simultaneously to the smallest detectable refractive index changes, exploring the

https://doi.org/10.1021/acsphotonics.5c01198
ACS Photonics XXXX, XXX, XXX−XXX

overall limits of the platform. In order to investigate this behavior, very small refractive index changes have to be realized in a controlled and reproducible way. In our experiments, we make use of the thermo-optic effect, that is, the dependence of the refractive index of a material on its temperature. In a setup as sketched in Figure 4b, setting a certain temperature, controlled by a PID feedback loop, allows us to very accurately choose a specific refractive index and thus also allows to finely tune this refractive index in ultimately small steps. To this end, we utilized a cell sketched in Figure 4a. A droplet of glycerol was trapped between a coverslip and a Mie void sample with a few layers of Kapton tape acting as a spacer and rim at the edges, sealed with glue. Glycerol as an analyte was chosen for its large thermo-optic coefficient of -2.3×10^{-4} (1/K).[67]

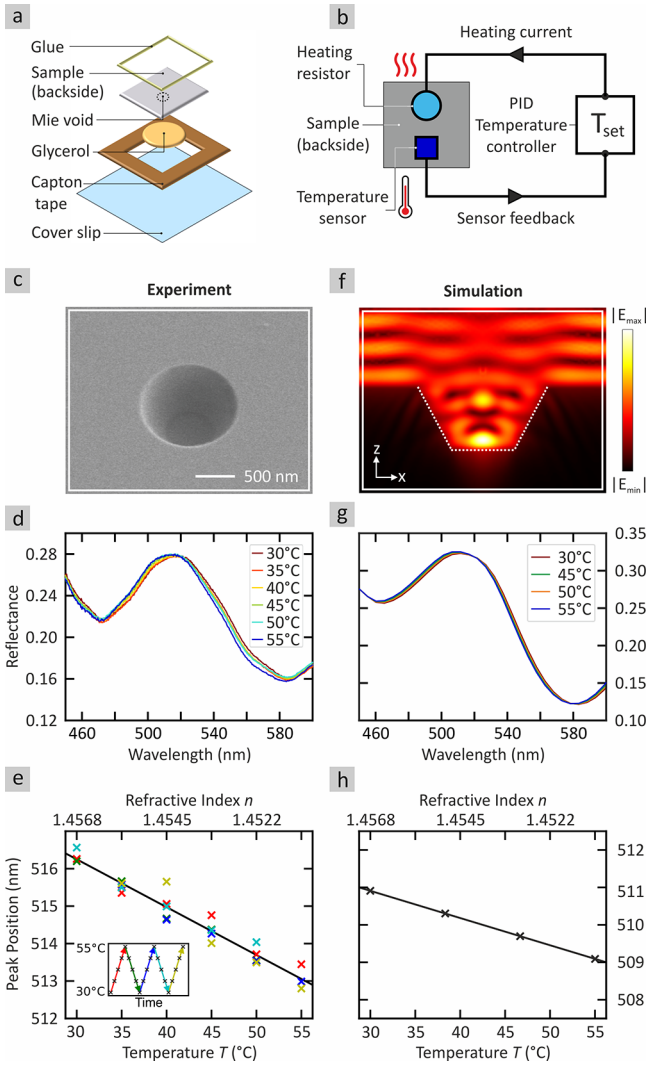

Figure 4. Ultimate limits of single Mie void-based refractive index sensing. (a) Sketch of the measurement cell. (b) Measurement scheme utilizing the thermo-optic coefficient of glycerol. Via a PID temperature controller, the sample and analyte temperature and thus the refractive index can be precisely controlled. (c) SEM micrograph of the measured Mie void. (d) Reflectance spectra of an individual glycerol-filled Mie void for temperatures between 30 and 55 °C. For clarity, only the average of all spectra at one temperature is plotted, making the small blue shift visible. (e) Extracted peak position versus the applied temperature and corresponding refractive index for a five-cycle-measurement and 26 individual spectra. A linear regression is applied to the data points to extract a sensitivity of $\Delta\lambda/\Delta n = (494 \pm 25)$nm/RIU. (f) Simulated electric field intensity distribution. (g) Simulated reflectance spectra corresponding to the experimental data in (d). (h) Simulated peak shift for the refractive index range covered in the experimental data in (e).

We performed single Mie void spectral measurements analogous to the previous measurements but now as a function of temperature, from which we can determine the corresponding refractive index via the thermo-optic coefficient as described in the Supporting Information.[67] The utilized Mie void displayed in the SEM image of Figure 4c has a top radius of 610 nm, a bottom radius of 295 nm, a depth of 600 nm, and a volume of 390 attoliters. For this single void, we measure spectra from 30 to 55 °C in steps of 5K, corresponding to a refractive index change of 1.15×10^{-3}. The cycling scheme is illustrated in the inset of Figure 4e consisting of five cycles between these extremal values (three times up, two times down) resulting in 26 individual spectra. For clarity not all 26, but the average of those measured at identical temperature, are displayed in Figure 4d (the full data is found in Figure S4 of the Supporting Information). A small blue shift of the spectra is visible as the temperature of the analyte is increased. In order to extract this spectral shift from the measured spectra we utilized the so-called centroid method.[27] This method is robust against noise as it takes a larger spectral region into account and is thus generally more suitable to detect very small spectral shifts.

In Figure 4e, we extract one centroid position per spectral measurement, resulting in three data points at the maximum and minimum temperature and five data points for each temperature setting in-between. The refractive index values on the upper horizontal axis were calculated via the thermo-optic coefficient of glycerol and the applied temperature (individual steps correspond to a refractive index change of just 1.15×10^{-3}).

The measurement clearly shows that the change in refractive index is imprinted on the optical properties and can thus be extracted. A blue shift in resonance position for increasing temperature is observable, which matches the negative sign of the thermo-optic coefficient of glycerol.[67] The slope of a linear fit to the data points yields a sensitivity of $\Delta\lambda/\Delta n = (494 \pm 25)$nm/RIU, comparable to the earlier measurements. In combination with the peak width at half prominence of 42 nm this constitutes a figure of merit of FOM = 11.8/RIU in a single void measurement of 390 attoliters sensing volume. We note that the observed blue shift for increased temperatures has to be attributed to the glycerol in the void with its negative thermo-optic coefficient and cannot be caused by a change in refractive index in the GaAs, as GaAs has a positive thermo-optic coefficient, which would cause a red shift. This demonstrates again that Mie voids are highly sensitive to the refractive index inside the void, as this is where the electric field is concentrated, with very little extending into the surrounding substrate. Figure 4f illustrates this by depicting the calculated electric field intensity distribution at resonance. As for Figure 3d the field distribution is one of a higher order mode due to the relatively significant size and high refractive index of the analyte. In Figure 4g, we plotted the simulated reflectance spectra for refractive indices between 1.4568 and 1.45102 (corresponding to 30 and 55 °C, respectively). The shape of the reflectance spectra as well as spectral position is in good agreement with the experiment. In Figure 4h, we have

https://doi.org/10.1021/acsphotonics.5c01198
ACS Photonics XXXX, XXX, XXX−XXX

drawn the simulated resonance shift over the refractive index, obtaining a sensitivity of $\Delta\lambda/\Delta n = 316$nm/RIU. The significant discrepancy might be due uncertainties in the measured void dimensions used for the simulation or an incomplete representation of the measurement system through simulation.The variation in the obtained spectral positions in Figure 4e demonstrates that we are very close to the detection limit of our sensing platform. Indeed, the slope of the shift in combination with this variation in spectral position for nominally identical measurements determines the detection limit of our platform, which is a key metric for most sensing applications. We thus calculate for each temperature the standard deviation of the peak positions and average over all six temperatures to determine a standard deviation in peak position of $\sigma = 0.26$ nm. By requiring a 2σ separation in peak position and taking into account the sensitivity of $\Delta\lambda/\Delta n = (494 \pm 25)$nm/RIU we deduce a smallest detectable refractive index shift of 1×10^{-3} RIU in a volume of 390 attoliters. This change in refractive index equals a 4K temperature change in our experiment

As we operate at the limit of our platform and are susceptible to noise, two additional iterations of this experiment are presented in the Supporting Information Figure S4 yielding similar results. To reach further insight on the limits of this method, Figure S5 explores the repeatability of nominally identical measurements after purposeful de- and realignment as well as de- and refocusing. Over six measurements the spread in peak position was below 0.5 nm with a standard deviation of 0.21 nm.

The practical implementation of attoliter-scale Mie void fluid sensing requires precise analyte delivery methods compatible with the ultrasmall sensing volume. Recent developments in nanofluidics have demonstrated scalable techniques for generating monodisperse droplets down to 30 attoliters using nanomicrofluidic geometries, with droplet size solely governed by the nanochannel height.[68] Additionally, integrated silicon microfluidic chips have been developed to segment analytes into picoliter-scale droplets and deposit them onto substrates with micrometer-scale accuracy, achieving attomole-level detection sensitivity.[69] Such platforms provide a viable path toward high-throughput and localized analyte delivery into Mie void arrays.

We finally mention that our system does not provide intrinsic material contrast suitable for biofunctionalization. There are, however, several possibilities to address this point for our platform. Electron beam lithography can be used to pattern anchor points on the bottom of the void (e.g., made of thin gold). Another approach might be based on the use of an electron beam patterned mask as utilized for quantum dot delivery on plasmonic Yagi-Uda antennas.[70]

CONCLUSIONS

In summary we have demonstrated the use of Mie voids as a sensing platform, making use of the full access to the modal field distribution as well as the well-defined and ultrasmall sensing volume on the order to a few hundred attoliters. Specifically, we observe sensitivities on the order of 300−550 nm/RIU, depending on the mode order, and, utilizing the thermo-optic effect, demonstrate refractive index discrimination down to 1×10^{-3} RIU in a volume of 390 attoliters. Extended mode sensing techniques show sizeably higher sensitivities, yet, have significantly larger or not such a well-defined sensing volume. Our ansatz is therefore ideal for the interrogation of ultrasmall analyte and material volumes, which can be straightforwardly filled into the cuvette, conveniently formed by the Mie void itself. In the future, functionalization can also add specificity,[16,71−74] moving beyond proof-of-concept refractive index sensing. Particularly interesting in our case is the incorporation of hydrogels and similar material classes into the void, again making use of the intrinsic full access to the field and therefore maximizing interaction and in turn sensitivity.[75] Also, the combination with microfluidics and the read out using a cheap CMOS color camera could render our ansatz very attractive for automated pharmaceutical and chemical analytics.

ASSOCIATED CONTENT

Supporting Information

The Supporting Information is available free of charge at https://pubs.acs.org/doi/10.1021/acsphotonics.5c01198.

Additional array sensing measurements (Figure S1), simulation exploring the difference between filling only the void volume with an analyte compared to only the half-space above as well as both (Figure S2), sensing measurement exploring the lower limits in sensing volume (Figure S3), calculation of the refractive index via the thermo-optic coefficient, additional iterations of the experiments presented in Figure 4 (Figure S4), test in repeatability of the single void measurement scheme (Figure S5), control experiment of the temperature-dependent measurements in empty voids (Figure S6), and demonstration of the impact of the real space aperture size (F stop) on the measured reflectance spectra as well as their reproducibility (Figure S7) (PDF)

AUTHOR INFORMATION

Corresponding Author

Serkan Arslan − *4th Physics Institute and Research Center SCoPE, University of Stuttgart, Stuttgart 70569, Germany;* orcid.org/0009-0001-3357-1972; Email: serkan.arslan@pi4.uni-stuttgart.de

Authors

Micha Kappel − *4th Physics Institute and Research Center SCoPE, University of Stuttgart, Stuttgart 70569, Germany*

Adrià Canós Valero − *Institute of Physics, University of Graz, and Nawi Graz, Graz 8010, Austria; Riga Technical University, Institute of Telecommunications, Riga 1048, Latvia*

Thi Thu Huong Tran − *4th Physics Institute and Research Center SCoPE, University of Stuttgart, Stuttgart 70569, Germany;* orcid.org/0009-0000-3567-2112

Julian Karst − *4th Physics Institute and Research Center SCoPE, University of Stuttgart, Stuttgart 70569, Germany*

Philipp Christ − *Institute of Physics, University of Graz, and Nawi Graz, Graz 8010, Austria*

Ulrich Hohenester − *Institute of Physics, University of Graz, and Nawi Graz, Graz 8010, Austria;* orcid.org/0000-0001-8929-2086

Thomas Weiss − *4th Physics Institute and Research Center SCoPE, University of Stuttgart, Stuttgart 70569, Germany; Institute of Physics, University of Graz, and Nawi Graz, Graz 8010, Austria;* orcid.org/0000-0002-4991-6779

https://doi.org/10.1021/acsphotonics.5c01198
ACS Photonics XXXX, XXX, XXX−XXX

Harald Giessen − *4th Physics Institute and Research Center SCoPE, University of Stuttgart, Stuttgart 70569, Germany;* orcid.org/0000-0002-4270-3850

Mario Hentschel − *4th Physics Institute and Research Center SCoPE, University of Stuttgart, Stuttgart 70569, Germany;* orcid.org/0000-0002-6882-4183

Complete contact information is available at: https://pubs.acs.org/10.1021/acsphotonics.5c01198

Notes

A preprint version of this work was published to arXiv on July 2. 2024: Serkan Arslan; Micha Kappel; Adrià Canós Valero; Thu Huong T. Tran; Julian Karst; Philipp Christ; Ulrich Hohenester; Thomas Weiss; Harald Giessen; Mario Hentschel; Attoliter Mie Void Sensing. 2024, 2407.02331. arXiv. 10.48550/arXiv.2407.02331 (accessed June 11, 2025).
The authors declare no competing financial interest.

■ ACKNOWLEDGMENTS

This work was supported the Ministerium für Wissenschaft, Forschung und Kunst Baden-Württemberg (RiSC Project "Mie Voids", ZAQuant), Vector Stiftung MINT-Innovationen, Baden-Württemberg-Stiftung (Opterial), European Research Council (ERC Advanced Grant Complexplas & ERC PoC Grant 3DPrintedOptics), and Bundesministerium für Bildung und Forschung, Deutsche Forschungsgemeinschaft (SPP1839 "Tailored Disorder" and GRK2642 "Towards Graduate Experts in Photonic Quantum Technologies"). A.C.V. acknowledges funding by the project No 1.1.1.9/LZP/1/24/101 : "Non-Hermitian physics of spatiotemporal photonic crystals of arbitrary shape (PROTOTYPE)".

■ REFERENCES

(1) Lal, S.; Link, S.; Halas, N. J. Nano-Optics from Sensing to Waveguiding. *Nat. Photonics* **2007**, *1* (11), 641−648.
(2) Anker, J. N.; Hall, W. P.; Lyandres, O.; Shah, N. C.; Zhao, J.; Van Duyne, R. P. Biosensing with Plasmonic Nanosensors. *Nat. Mater.* **2008**, *7*, 442−453.
(3) Mayer, K. M.; Hafner, J. H. Localized Surface Plasmon Resonance Sensors. *Chem. Rev.* **2011**, *111* (6), 3828−3857.
(4) Altug, H.; Oh, S.-H.; Maier, S. A.; Homola, J. Advances and Applications of Nanophotonic Biosensors. *Nat. Nanotechnol.* **2022**, *17* (1), 5−16.
(5) Semenyshyn, R.; Hentschel, M.; Stanglmair, C.; Teutsch, T.; Tarin, C.; Pacholski, C.; Giessen, H.; Neubrech, F. In Vitro Monitoring Conformational Changes of Polypeptide Monolayers Using Infrared Plasmonic Nanoantennas. *Nano Lett.* **2019**, *19* (1), 1−7.
(6) Aksu, S.; Yanik, A. A.; Adato, R.; Artar, A.; Huang, M.; Altug, H. High-Throughput Nanofabrication of Infrared Plasmonic Nano-antenna Arrays For. Vibrational Nanospectroscopy. *Nano Lett.* **2010**, *10* (7), 2511−2518.
(7) Rodrigo, D.; Limaj, O.; Janner, D.; Etezadi, D.; Garcia de Abajo, F. J.; Pruneri, V.; Altug, H. Mid-Infrared Plasmonic Biosensing with Graphene. *Science* **2015**, *349* (6244), 165−168.
(8) Solomon, M. L.; Saleh, A. A. E.; Poulikakos, L. V.; Abendroth, J. M.; Tadesse, L. F.; Dionne, J. A. Nanophotonic Platforms for Chiral Sensing and Separation. *Acc. Chem. Res.* **2020**, *53* (3), 588−598.
(9) Larsson, E. M.; Langhammer, C.; Zorić, I.; Kasemo, B. Nanoplasmonic Probes of Catalytic Reactions. *Science* **2009**, *326* (5956), 1091−1094.
(10) Maksimov, D. N.; Gerasimov, V. S.; Romano, S.; Polyutov, S. P. Refractive Index Sensing with Optical Bound States in the Continuum. *Opt. Express* **2020**, *28* (26), 38907.
(11) Both, S.; Weiss, T. Resonant States and Their Role in Nanophotonics. *Semicond. Sci. Technol.* **2022**, *37* (1), No. 013002.
(12) Maksimov, D. N.; Gerasimov, V. S.; Bogdanov, A. A.; Polyutov, S. P. Enhanced Sensitivity of an All-Dielectric Refractive Index Sensor with an Optical Bound State in the Continuum. *Phys. Rev. A* **2022**, *105* (3), No. 033518.
(13) Zhang, W.; Martin, O. J. F. A Universal Law for Plasmon Resonance Shift in Biosensing. *ACS Photonics* **2015**, *2* (1), 144−150.
(14) Yang, J.; Giessen, H.; Lalanne, P. Simple Analytical Expression for the Peak-Frequency Shifts of Plasmonic Resonances for Sensing. *Nano Lett.* **2015**, *15* (5), 3439−3444.
(15) Gao, B.; Wang, Y.; Zhang, T.; Xu, Y.; He, A.; Dai, L.; Zhang, J. Nanoscale Refractive Index Sensors with High Figures of Merit via Optical Slot Antennas. *ACS Nano* **2019**, *13* (8), 9131−9138.
(16) Aćimović, S. S.; Ortega, M. a; Sanz, V.; Berthelot, J.; Garcia-Cordero, J. L.; Renger, J.; Maerkl, S. J.; Kreuzer, M. P.; Quidant, R. LSPR Chip for Parallel, Rapid, and Sensitive Detection of Cancer Markers in Serum. *Nano Lett.* **2014**, *14* (5), 2636−2641.
(17) Zhan, Y.; Lei, D. Y.; Li, X.; Maier, S. A. Plasmonic Fano Resonances in Nanohole Quadrumers for Ultra-Sensitive Refractive Index Sensing. *Nanoscale* **2014**, *6* (9), 4705−4715.
(18) Khalavka, Y.; Becker, J.; Sönnichsen, C. Synthesis of Rod-Shaped Gold Nanorattles with Improved Plasmon Sensitivity and Catalytic Activity. *J. Am. Chem. Soc.* **2009**, *131* (5), 1871−1875.
(19) Wang, J.; Kühne, J.; Karamanos, T.; Rockstuhl, C.; Maier, S. A.; Tittl, A. All-Dielectric Crescent Metasurface Sensor Driven by Bound States in the Continuum. *Adv. Funct. Mater.* **2021**, *31* (46), 1−10.
(20) Chong, K. E.; Orton, H. W.; Staude, I.; Decker, M.; Miroshnichenko, A. E.; Brener, I.; Kivshar, Y. S.; Neshev, D. N. Refractive Index Sensing with Fano Resonances in Silicon Oligomers. *Philos. Trans. R. Soc. A Math. Phys. Eng. Sci.* **2017**, *375* (2090), 20160070.
(21) Kristensen, P. T.; Herrmann, K.; Intravaia, F.; Busch, K. Modeling Electromagnetic Resonators Using Quasinormal Modes. *Adv. Opt. Photonics* **2020**, *12* (3), 612.
(22) Aćimović, S. S.; Kreuzer, M. P.; González, M. U.; Quidant, R. Plasmon Near-Field Coupling in Metal Dimers as a Step toward Single-Molecule Sensing. *ACS Nano* **2009**, *3* (5), 1231−1237.
(23) Neubrech, F.; Beck, S.; Glaser, T.; Hentschel, M.; Giessen, H.; Pucci, A. Spatial Extent of Plasmonic Enhancement of Vibrational Signals in the Infrared. *ACS Nano* **2014**, *8* (6), 6250−6258.
(24) Larsson, E. M.; Syrenova, S.; Langhammer, C. Nanoplasmonic Sensing for Nanomaterials Science. *Nanophotonics* **2012**, *1* (3−4), 249−266.
(25) Nugroho, F. A. A.; Bai, P.; Darmadi, I.; Castellanos, G. W.; Fritzsche, J.; Langhammer, C.; Gómez Rivas, J.; Baldi, A. Inverse Designed Plasmonic Metasurface with Parts per Billion Optical Hydrogen Detection. *Nat. Commun.* **2022**, *13* (1), 5737.
(26) Sterl, F.; Strohfeldt, N.; Both, S.; Herkert, E.; Weiss, T.; Giessen, H. Design Principles for Sensitivity Optimization in Plasmonic Hydrogen Sensors. *ACS Sensors* **2020**, *5* (4), 917−927.
(27) Dahlin, A. B.; Tegenfeldt, J. O.; Höök, F. Improving the Instrumental Resolution of Sensors Based on Localized Surface Plasmon Resonance Interfacial Refractive Index of Nanoscale Noble Metal Generic Data Analysis Algorithms and a Simple Experimen-Comparable to That of State-of-the Art SPR Systems. *Anal. Chem.* **2006**, *78* (13), 4416−4423.
(28) Tittl, A.; Leitis, A.; Liu, M.; Yesilkoy, F.; Choi, D. Y.; Neshev, D. N.; Kivshar, Y. S.; Altug, H. Imaging-Based Molecular Barcoding with Pixelated Dielectric Metasurfaces. *Science* **2018**, *360* (6393), 1105−1109.
(29) Gallinet, B.; Martin, O. J. F. Refractive Index Sensing with Subradiant Modes: A Framework To Reduce Losses in Plasmonic Nanostructures. *ACS Nano* **2013**, *7* (8), 6978−6987.
(30) García-Guirado, J.; Svedendahl, M.; Puigdollers, J.; Quidant, R. Enantiomer-Selective Molecular Sensing Using Racemic Nano-plasmonic Arrays. *Nano Lett.* **2018**, *18* (10), 6279−6285.
(31) Gunnarsson, L.; Bjerneld, E. J.; Xu, H.; Petronis, S.; Kasemo, B.; Käll, M. Interparticle Coupling Effects in Nanofabricated

Substrates for Surface-Enhanced Raman Scattering. *Appl. Phys. Lett.* **2001**, *78* (6), 802−804.
(32) West, J. L.; Halas, N. J. Engineered Nanomaterials for Biophotonics Applications: Improving Sensing, Imaging, and Therapeutics. *Annu. Rev. Biomed. Eng.* **2003**, *5*, 285−292.
(33) Tittl, A.; Giessen, H.; Liu, N. Plasmonic Gas and Chemical Sensing. *Nanophotonics* **2014**, *3* (3), 157−180.
(34) Mesch, M.; Weiss, T.; Schäferling, M.; Hentschel, M.; Hegde, R. S.; Giessen, H. Highly Sensitive Refractive Index Sensors with Plasmonic Nanoantennas−Utilization of Optimal Spectral Detuning of Fano Resonances. *ACS Sensors* **2018**, *3* (5), 960−966.
(35) Lalanne, P.; Yan, W.; Vynck, K.; Sauvan, C.; Hugonin, J. Light Interaction with Photonic and Plasmonic Resonances. *Laser Photon. Rev.* **2018**, *12* (5), 1700113.
(36) Svedendahl, M.; Chen, S.; Dmitriev, A.; Käll, M. Refractometric Sensing Using Propagating versus Localized Surface Plasmons: A Direct Comparison. *Nano Lett.* **2009**, *9* (12), 4428−4433.
(37) Aigner, A.; Tittl, A.; Wang, J.; Weber, T.; Kivshar, Y.; Maier, S. A.; Ren, H. Plasmonic Bound States in the Continuum to Tailor Light-Matter Coupling. *Sci. Adv.* **2022**, *8* (49), 1−8.
(38) Awazu, K.; Rockstuhl, C.; Fujimaki, M.; Fukuda, N.; Tominaga, J.; Komatsubara, T.; Ikeda, T.; Ohki, Y. High Sensitivity Sensors Made of Perforated Waveguides. *Opt. Express* **2007**, *15* (5), 2592.
(39) Zhou, W.; Odom, T. W. Tunable Subradiant Lattice Plasmons by Out-of-Plane Dipolar Interactions. *Nat. Nanotechnol.* **2011**, *6* (7), 423−427.
(40) McMahon, J. M.; Henzie, J.; Odom, T. W.; Schatz, G. C.; Gray, S. K. Tailoring the Sensing Capabilities of Nanohole Arrays in Gold Films with Rayleigh Anomaly-Surface Plasmon Polaritons. *Opt. Express* **2007**, *15* (26), 18119.
(41) Weiss, T.; Mesch, M.; Schäferling, M.; Giessen, H.; Langbein, W.; Muljarov, E. A. From Dark to Bright: First-Order Perturbation Theory with Analytical Mode Normalization for Plasmonic Nanoantenna Arrays Applied to Refractive Index Sensing. *Phys. Rev. Lett.* **2016**, *116* (23), No. 237401.
(42) Evans, P. R.; Wurtz, G. A.; Atkinson, R.; Hendren, W.; O'Connor, D.; Dickson, W.; Pollard, R. J.; Zayats, A. V. Plasmonic Core/Shell Nanorod Arrays: Subattoliter Controlled Geometry and Tunable Optical Properties. *J. Phys. Chem. C* **2007**, *111* (34), 12522−12527.
(43) Foreman, M. R.; Swaim, J. D.; Vollmer, F. Whispering Gallery Mode Sensors. *Adv. Opt. Photonics* **2015**, *7* (2), 168.
(44) Liu, W.; Chen, Y. L.; Tang, S. J.; Vollmer, F.; Xiao, Y. F. Nonlinear Sensing with Whispering-Gallery Mode Microcavities: From Label-Free Detection to Spectral Fingerprinting. *Nano Lett.* **2021**, *21* (4), 1566−1575.
(45) Enoch, S.; Quidant, R.; Badenes, G. Optical Sensing Based on Plasmon Coupling in Nanoparticle Arrays. *Opt. Express* **2004**, *12* (15), 3422.
(46) Ameling, R.; Langguth, L.; Hentschel, M.; Mesch, M.; Braun, P. V.; Giessen, H. Cavity-Enhanced Localized Plasmon Resonance Sensing. *Appl. Phys. Lett.* **2010**, *97* (25), 253116.
(47) Bosio, N.; Šípová-Jungová, H.; Länk, N. O.; Antosiewicz, T. J.; Verre, R.; Käll, M. Plasmonic versus All-Dielectric Nanoantennas for Refractometric Sensing: A Direct Comparison. *ACS Photonics* **2019**, *6* (6), 1556−1564.
(48) Bozzola, A.; Perotto, S.; De Angelis, F. Hybrid Plasmonic-Photonic Whispering Gallery Mode Resonators for Sensing: A Critical Review. *Analyst* **2017**, *142* (6), 883−898.
(49) Dantham, V. R.; Holler, S.; Barbre, C.; Keng, D.; Kolchenko, V.; Arnold, S. Label-Free Detection of Single Protein Using a Nanoplasmonic-Photonic Hybrid Microcavity. *Nano Lett.* **2013**, *13* (7), 3347−3351.
(50) Kuznetsov, A. I.; Miroshnichenko, A. E.; Brongersma, M. L.; Kivshar, Y. S.; Luk'yanchuk, B. Optically Resonant Dielectric Nanostructures. *Science* **2016**, *354* (6314), 2472.
(51) Hentschel, M.; Koshelev, K.; Sterl, F.; Both, S.; Karst, J.; Shamsafar, L.; Weiss, T.; Kivshar, Y.; Giessen, H. Dielectric Mie Voids: Confining Light in Air. *Light Sci. Appl.* **2023**, *12* (1), 3.
(52) Hamidi, M.; Koshelev, K.; Gladyshev, S.; Valero, A. C.; Hentschel, M.; Giessen, H.; Kivshar, Y.; Weiss, T. Quasi-Babinet Principle in Dielectric Resonators and Mie Voids. *Phys. Rev. Res.* **2025**, *7* (1), No. 013136.
(53) Mann, S. A.; Grote, R. R.; Osgood, R. M.; Schuller, J. A. Dielectric Particle and Void Resonators for Thin Film Solar Cell Textures. *Opt. Express* **2011**, *19* (25), 25729.
(54) Stewart, M. E.; Anderton, C. R.; Thompson, L. B.; Maria, J.; Gray, S. K.; Rogers, J. a; Nuzzo, R. G. Nanostructured Plasmonic Sensors. *Chem. Rev.* **2008**, *108* (2), 494−521.
(55) Chen, Y.; Ming, H. Review of Surface Plasmon Resonance and Localized Surface Plasmon Resonance Sensor. *Photonic Sensors* **2012**, *2* (1), 37−49.
(56) Prasad, A.; Choi, J.; Jia, Z.; Park, S.; Gartia, M. R. Nanohole Array Plasmonic Biosensors: Emerging Point-of-Care Applications. *Biosens. Bioelectron.* **2019**, *130*, 185−203.
(57) Li, X.; Soler, M.; Özdemir, C. I.; Belushkin, A.; Yesilköy, F.; Altug, H. Plasmonic Nanohole Array Biosensor for Label-Free and Real-Time Analysis of Live Cell Secretion. *Lab Chip* **2017**, *17* (13), 2208−2217.
(58) Reiter, S.; Han, W.; Mai, C.; Spirito, D.; Jose, J.; Zöllner, M.; Fursenko, O.; Schubert, M. A.; Stemmler, I.; Wenger, C.; Fischer, I. A. Titanium Nitride Plasmonic Nanohole Arrays for CMOS-Compatible Integrated Refractive Index Sensing: Influence of Layer Thickness on Optical Properties. *Plasmonics* **2023**, *18* (3), 831−843.
(59) Garoli, D.; Yamazaki, H.; Maccaferri, N.; Wanunu, M. Plasmonic Nanopores for Single-Molecule Detection and Manipulation: Toward Sequencing Applications. *Nano Lett.* **2019**, *19* (11), 7553−7562.
(60) Jackman, J. A.; Linardy, E.; Yoo, D.; Seo, J.; Ng, W. B.; Klemme, D. J.; Wittenberg, N. J.; Oh, S.; Cho, N. Plasmonic Nanohole Sensor for Capturing Single Virus-Like Particles toward Virucidal Drug Evaluation. *Small* **2016**, *12* (9), 1159−1166.
(61) Yanik, A. A.; Huang, M.; Artar, A.; Chang, T.; Altug, H. Integrated Nanoplasmonic-Nanofluidic Biosensors with Targeted Delivery of Analytes Integrated. *Appl. Phys. Lett.* **2010**, *96*, No. 021101.
(62) Yavas, O.; Svedendahl, M.; Dobosz, P.; Sanz, V.; Quidant, R. On-a-Chip Biosensing Based on All-Dielectric Nanoresonators. *Nano Lett.* **2017**, *17* (7), 4421−4426.
(63) Sarbajna, A.; Danielsen, D. R.; Casses, L. N.; Stenger, N.; Bøggild, P.; Raza, S. Encapsulated Void Resonators in Van Der Waals Heterostructures. *Laser Photon. Rev.* **2025**, *19* (3), No. 2401215.
(64) Moutzouris, K.; Papamichael, M.; Betsis, S. C.; Stavrakas, I.; Hloupis, G.; Triantis, D. Refractive, Dispersive and Thermo-Optic Properties of Twelve Organic Solvents in the Visible and near-Infrared. *Appl. Phys. B: Laser Opt.* **2014**, *116* (3), 617−622.
(65) Kedenburg, S.; Vieweg, M.; Gissibl, T.; Giessen, H. Linear Refractive Index and Absorption Measurements of Nonlinear Optical Liquids in the Visible and Near-Infrared Spectral Region. *Opt. Mater. Express* **2012**, *2* (11), 1588.
(66) Sterl, F.; Herkert, E.; Both, S.; Weiss, T.; Giessen, H. Shaping the Color and Angular Appearance of Plasmonic Metasurfaces with Tailored Disorder. *ACS Nano* **2021**, *15* (6), 10318−10327.
(67) Cao, Z.; Jiang, L.; Wang, S.; Wang, M.; Liu, D.; Wang, P.; Zhang, F.; Lu, Y. All-Glass Extrinsic Fabry−Perot Interferometer Thermo-Optic Coefficient Sensor Based on a Capillary Bridged Two Fiber Ends. *Appl. Opt.* **2015**, *54* (9), 2371.
(68) Shui, L.; van den Berg, A.; Eijkel, J. C. T. Scalable Attoliter Monodisperse Droplet Formation Using Multiphase Nano-Microfluidics. *Microfluid. Nanofluidics* **2011**, *11* (1), 87−92.
(69) Shi, W.; Bell, S.; Iyer, H.; Brenden, C. K.; Zhang, Y.; Kim, S.; Park, I.; Bashir, R.; Sweedler, J.; Vlasov, Y. Integrated Silicon Microfluidic Chip for Picoliter-Scale Analyte Segmentation and Microscale Printing for Mass Spectrometry Imaging. *Lab Chip* **2022**, *23* (1), 72−80.
(70) Curto, A. G.; Volpe, G.; Taminiau, T. H.; Kreuzer, M. P.; Quidant, R.; van Hulst, N. F. Unidirectional Emission of a Quantum Dot Coupled to a Nanoantenna. *Science* **2010**, *329* (5994), 930−933.

https://doi.org/10.1021/acsphotonics.5c01198
ACS Photonics XXXX, XXX, XXX−XXX

(71) Rosman, C.; Prasad, J.; Neiser, A.; Henkel, A.; Edgar, J.; Sönnichsen, C. Multiplexed Plasmon Sensor for Rapid Label-Free Analyte Detection. *Nano Lett.* **2013**, *13* (7), 3243−3247.
(72) Dahlin, A.; Zäch, M.; Rindzevicius, T.; Käll, M.; Sutherland, D. S.; Höök, F. Localized Surface Plasmon Resonance Sensing of Lipid-Membrane-Mediated Biorecognition Events. *J. Am. Chem. Soc.* **2005**, *127* (14), 5043−5048.
(73) Karawdeniya, B. I.; Damry, A. M.; Murugappan, K.; Manjunath, S.; Bandara, Y. M. N. D. Y.; Jackson, C. J.; Tricoli, A.; Neshev, D. Surface Functionalization and Texturing of Optical Metasurfaces for Sensing Applications. *Chem. Rev.* **2022**, *122* (19), 14990−15030.
(74) Bontempi, N.; Chong, K. E.; Orton, H. W.; Staude, I.; Choi, D. Y.; Alessandri, I.; Kivshar, Y. S.; Neshev, D. N. Highly Sensitive Biosensors Based on All-Dielectric Nanoresonators. *Nanoscale* **2017**, *9* (15), 4972−4980.
(75) Mesch, M.; Zhang, C.; Braun, P. V.; Giessen, H. Functionalized Hydrogel on Plasmonic Nanoantennas for Noninvasive Glucose Sensing. *ACS Photonics* **2015**, *2* (4), 475−480.

https://doi.org/10.1021/acsphotonics.5c01198
ACS Photonics XXXX, XXX, XXX−XXX